Advanced Steel Construction – Vol. 22 No. 3 (2026) 275–285
DOI:10.18057/IJASC.2026.22.3.3

HYSTERETIC BEHAVIOR OF H-SECTION ALUMINUM ALLOY MEMBERS UNDER AXIAL LOADING: EXPERIMENTAL AND NUMERICAL STUDY

Xiao-Nong Guo [1], Yin Zou [1] and Xing-Ye Wang [2, *]

[1] *College of Civil Engineering, Tongji University, Shanghai 200092, China*
[2] *Railway Engineering Research Institute, China Academy of Railway Sciences Corporation Limited, Beijing 100081, China*
* *(Corresponding author: E-mail: wang_xingye163@163.com)*

A B S T R A C T

This study investigates the hysteretic behavior of aluminum alloy members in gusset joint latticed shells. Due to the low elastic modulus of aluminum alloys and the weak-axis buckling susceptibility of H-shaped members, their hysteretic behavior is complex. However, studies remain limited, particularly on their axial compression and tension behavior under varying buckling modes.The research combines experimental and numerical approaches. Hysteretic loading tests were conducted on 11 aluminum alloy members under axial loading. A refined finite element (FE) model was developed to simulate the process, followed by a pin-ended member model for parametric analysis considering slenderness ratio, cross-sectional parameters, initial geometric imperfection, and tensile/compressive displacement amplitudes. A multi-scale latticed shell model was then constructed to evaluate the effectiveness of segmented beam elements in capturing hysteresis. Results show that compression buckling significantly reduces bearing capacity, though tensile loading mitigates residual deformation. Higher slenderness ratios and greater initial imperfections worsen post-buckling degradation and alter hysteresis curves. The multi-scale analysis confirms the accuracy of the four-segment B32OS beam element in modeling hysteresis. This study addresses a gap in hysteretic behavior research of aluminum alloy members and provides essential data and modeling guidance for the seismic design of aluminum alloy latticed shells.

A R T I C L E   H I S T O R Y

Received: 30 April 2025
Revised: 17 September 2025
Accepted: 20 September 2025

K E Y W O R D S

Aluminum alloy members;
Cyclic loading;
Hysteretic behavior;
Finite element simulation;
Numerical Simulation;
Beam elements

1. Introduction

Aluminum alloy gusset joint latticed shells are a novel spatial structural system known for their aesthetic appeal, corrosion resistance, and lightweight properties, increasingly used in engineering applications [1][2]. As a spatial truss structure, the members of single-layer spherical latticed shells primarily bear axial compression under static loads such as dead and live loads. However, under horizontal seismic action, latticed shells undergo cyclic dynamic loading and out-of-plane vibration, with members bearing substantial axial force and bending moment. Given that the elastic modulus of aluminum alloys is only one-third that of steel, aluminum alloy members exhibit lower buckling bearing capacity under compression-bending action compared to steel members. Additionally, aluminum alloy members are industrially extruded profiles, often with H-section shapes, where significant differences in moment of inertia between strong and weak axes make them prone to buckling about the weak axis.

Extensive research has been conducted on the static behavior of aluminum alloy members.The earliest axial compression experiments can be traced back to Osgood and Holt in the 1930s [3][4]. Today, design codes in many countries provide mature formulations for calculating the bearing capacity of axially compressed or compression–bending aluminum alloy members [5]. Over the past decade, researchers such as Guo et al.[6] performed axial compression tests on 63 profiled aluminum alloy members, creating column curves for stability calculations. Liu et al.[7][8] investigated the compressive bearing capacity and failure modes of H-type aluminum alloy members with web openings by using experimental, numerical, and theoretical methods, analyzed the effects of opening parameters, cross-section dimensions, and slenderness ratios on the bearing capacity of the members, and gave the calculation methods. Zhu et al.[9] analyzed in-plane stability considering the stiffness of aluminum alloy gusset joints and adjacent member constraints, determining the effective lengths. Sun et al.[10] studied axial compression performance under various boundary conditions for H-section aluminum alloy members with initial curvature and torsional angles, observing flexural-torsional buckling failure. Moreover, Wang et al.[11][12][13] and Adeoti [14] conducted extensive experimental studies and finite element analyses on the flexural buckling and local buckling behavior of I-section, rectangular hollow section, and circular hollow section members. They compared the analysis results with existing design standards and found that most current design codes tend to be conservative for symmetric section members. Overall, researchers have conducted in-depth and systematic studies on aluminum alloy axially compressed members, bending members, and beam-column members, particularly symmetric section members. The bearing capacity calculation methods for these members have become relatively mature, leading to the development of relevant design codes [15].

Current research on the hysteretic behavior of aluminum alloys primarily focuses on the material and joint behavior. Regarding the hysteretic behavior of aluminum alloy materials, Guo et al. [16] conducted cyclic loading tests and fitted the monotonic loading curves, backbone curves, and hysteresis curves of 6082-T6 and 7020-T6 aluminum alloys, proposing a uniaxial hysteretic constitutive model for Chinese aluminum alloys and verifying its reliability. Pisapia [17], Branco[18], Kyriakos[19], and others investigated the low-cycle fatigue behavior and hysteretic constitutive models of various aluminum alloys through low-cyclic loading tests and theoretical analyses. For the hysteretic behavior of aluminum alloy joints, Guo [20], Wu [21], Xu [22], and Liu [23] conducted extensive experimental studies, investigating the failure modes, bearing capacity, deformation capacity, and energy dissipation capacity of gusset joints with different member cross-sections and joint configurations.

In contrast, research on the hysteretic behavior of aluminum alloy members remains scarce. Chen et al. [24] used finite element analysis to investigate the effects of alloy type and slenderness ratio on the hysteretic behavior of aluminum alloy axially compressed members. The results showed that, for the same slenderness ratio, the hysteretic behavior of 6061-T6 was superior to that of 6061-T4. Additionally, specimens with smaller slenderness ratios exhibited better performance under cyclic loading. Wu et al.[25] conducted eccentric cyclic loading tests on three H-shaped 6061-T6 aluminum alloy members with different slenderness ratios. They further used finite element (FE) model to study the effects of cross-section, slenderness ratio, and eccentricity. The results indicated that local buckling occurred first, followed by crack initiation at the buckled region, with cracks gradually propagating until the members fractured. However, due to the small slenderness ratios of the tested specimens, no global instability failure was observed. Thus, experimental research on the hysteretic behavior of the members experiencing global instability is still lacking, highlighting the need for further studies.

Several hysteretic models have been proposed for circular tubes under compression buckling and tension strengthening [26][27][28], yet these are often complex to implement and insufficiently accurate, being suitable only for single buckling modes. For H-sections prone to multiple modes, FE methods remain more adaptable. Prior works [29][30] commonly adopted beam element B31OS to represent aluminum alloy members in multi-scale models. In this study, members are subdivided into multiple beam elements to simulate buckling and hysteretic behavior, clarifying the simulation accuracy under various initial geometric imperfections and complex loading conditions.

Due to the current lack of research on the hysteretic behavior and simulation methods of aluminum alloy members during overall buckling, this study combined experimental loading tests with numerical simulations to investigate the hysteretic behavior of H-section members. First, axial loading hysteretic experiments were conducted on aluminum alloy members. Then, refined FE models were developed to simulate the loading process, with the simulation accuracy verified against the experimental data. On this basis, FE models with pin-ended member were established, and a parametric analysis was performed to investigate the effects of key parameters on the hysteretic behavior of the members. Finally, the beam elements intended for use in the multi-scale latticed shell model were studied using both single-member and multi-scale models to determine the appropriate number of element divisions and the accuracy of numerical simulation. The novelty of this study lies in experimentally capturing global instability of aluminum alloy members and validating a multi-segment beam element model against shell simulations.

2. Experimental study

2.1. Overview of the experiment

2.1.1. Objective of the experiment

This experiment primarily focused on collecting load and displacement data to assess the stress state and geometric configuration of the members. The study examined the hysteretic loading process of aluminum alloy members, exploring the impact of slenderness ratio and loading protocols on hysteretic behavior. Additionally, the hysteresis curves obtained from the experiment were used to evaluate the accuracy of subsequent FE models.

2.1.2. Specimen design

Due to the poor weldability of aluminum alloys and significant degradation in material properties in the heat-affected zone, the weld zone tends to fracture prematurely under tension. Therefore, bolted connections were employed at the member ends. To avoid premature fracture at the bolted connection, a dog-bone-shaped specimen was designed, reducing the flange width in the middle segment with a linear transition at the variable cross-section. The schematic diagrams of the specimens are shown in Fig. 1.

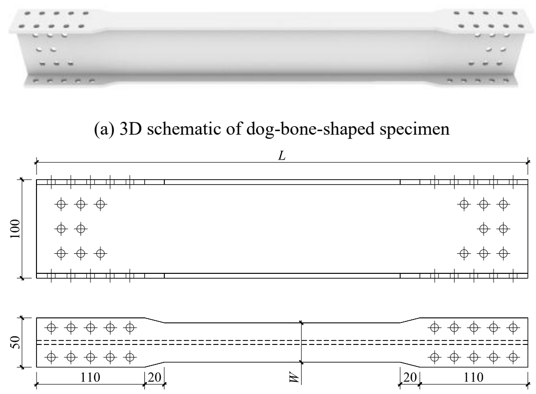

(a) 3D schematic of dog-bone-shaped specimen

(b) Specimen's dimension

Fig. 1 Dog-bone-shaped specimen

Table 1
Specimen parameters

Specimen ID	Length L (mm)	Flange Width W (mm)	Loading Protocol
YSY-1	1000	50	Pretest - Monotonic Loading
YSY-2	1000	50	Pretest - Single-Cycle Hysteretic
YSY-3	1000	50	Pretest - Multi-Cycle Hysteretic
L1200-TestA	1200	40	Hysteretic Loading
L1200-TestB	1200	40	Hysteretic Loading
L1000-TestA	1000	40	Hysteretic Loading
L1000-TestB	1000	40	Hysteretic Loading
L700-TestA	700	35	Hysteretic Loading
L700-TestB	700	35	Hysteretic Loading
L500-TestA	500	30	Hysteretic Loading
L500-TestB	500	30	Hysteretic Loading

The cross-sectional specification of the aluminum alloy members in the loading test was H100×50×4×5, made of aluminum alloy 6061-T6. The specimen parameters are listed in Table 1. Variables included member length and loading protocols. Hysteretic loading was applied to specimens with lengths of 1200 mm, 1000 mm, 700 mm, and 500 mm, with two loading protocols for each length. The flange widths of the middle segment were 40 mm, 40 mm, 35 mm, and 30 mm, respectively. Three pretests were conducted before the formal experiment: monotonic loading, single-cycle hysteretic loading, and multi-cycle hysteretic loading. The objective was to confirm the loading capacity of the setup, validate displacement measurement methods, and optimize the experimental procedure.

2.1.3. Material properties

The aluminum alloy members were made of 6061-T6 aluminum alloy. According to the standard "Metal Materials Tensile Test Part 1: Room Temperature Test Method" (GB/T 228.1-2021) [31], four material specimens were prepared by sampling from the same batch of aluminum alloy members, two from the flanges and two from the web.

The material test results are shown in Fig. 2 and Table 2. The statistical results are the nominal stress and strain of the material, which need to be converted into true stress and strain according to the following formula when performing numerical analysis[32].

$$\varepsilon_{\text{ture}} = \ln(1+\varepsilon_{\text{nom}}) \tag{1}$$

$$\sigma_{\text{ture}} = \sigma_{\text{nom}}(1+\varepsilon_{\text{nom}}) \tag{2}$$

Where ε_{nom} and σ_{nom} are nominal stress and strain, $\varepsilon_{\text{ture}}$ and σ_{ture} are ture stress and strain.

The table includes E (elastic modulus), $f_{0.2}$ (proof strength at 0.2% non-proportional extension), f_u (ultimate strength), and ε_u (ultimate strain). The elastic modulus of the flanges was slightly higher than that of the web, while the ultimate strain and 0.2% proof strength were slightly lower. The difference in ultimate stress between the two was within 0.4%. Overall, the material properties of the flanges and the web were essentially consistent, allowing for the use of the same material parameters.

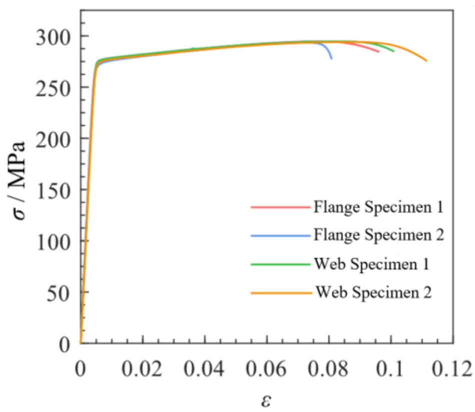

Fig. 2 Stress-strain curve of material test

Table 2
Summary of material property test results

Specimen	E / MPa	$f_{0.2}$ / MPa	f_u / MPa	ε_u
Flange Specimen 1	65629	273.8	294.6	0.096
Flange Specimen 2	63943	272.5	293.4	0.081
Web Specimen 1	61828	276.4	294.6	0.101
Web Specimen 2	62354	274.7	294.1	0.112

2.1.4. Setup of the experiment

Hysteretic tests require both tension and compression; thus, the support connections needed special design. The schematic of the experimental setup is shown in Fig. 3. The boundary conditions were conFig.d such that the upper and lower ends were rigidly connected around the strong axis, preventing rotation and lateral displacement. The weak axis was hinged, with an ear plate and pin connection at the lower end and a single-acting hinged connection to the actuator at the upper end. Both the top and lower ends were made of Q235 steel. Two stiffening ribs were welded to the top end's connection plate to enhance its bending stiffness, and four M36 high-strength bolts were used to connect it to the actuator. Similarly, two stiffening ribs were added to the ear plates of the lower end to prevent rotation about the strong axis, and four M36 high-strength bolts were used to connect it to the test platform. The aluminum alloy members were connected to the top and lower ends using 28 M10 high-strength bolts. The loading system consists of a 200 kN electro-hydraulic servo actuator equipped with displacement and force sensors. The displacement control accuracy was 0.01 mm, and the load control accuracy was 0.01 kN. The pretests verified that the lateral stiffness of the actuator was sufficient, making additional horizontal support unnecessary. Furthermore, there was no plastic shear deformation in the bolts, confirming sufficient connection bearing capacity.

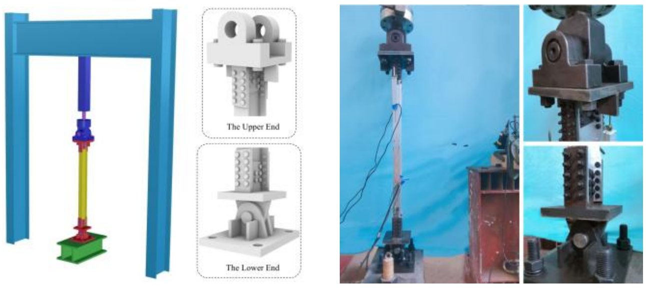

(a) Schematic of experimental setup (b) Actual experimental setup

Fig. 3 Setup of the experiment

2.1.5. Loading protocol

The hysteretic loading protocol adopted a dual control approach, utilizing displacement and load criteria. During compression, displacement was the primary control target. During tension, displacement was prioritized with load as a secondary criterion. In the initial compression stage, load control was applied until approaching the peak load, then switched to displacement control until reaching the target displacement. In tension, load control was used initially, switching to displacement control near the ultimate load to prevent premature fracture due to the poor ductility of aluminum alloys.

Two loading protocols, Test A and Test B, were employed. The two loading protocols have the same amplitude as shown in Fig. 5 a. The difference is that the TestA loading system only loads once per displacement level; the TestB loading system repeats loading twice per displacement level.

2.1.6. Layout of measurement point

The primary objective of this experiment was to investigate the relationship between the vertical deformation and vertical load of the members and to plot the hysteresis curves. The vertical load was recorded using the force sensor of the actuator, which simultaneously measured the displacement at the actuator's loading end. However, the actuator displacement included numerous complex factors, such as deformation of the reaction frame, deformation of the connection supports, and various gaps. Additionally, it encompassed the vertical displacement at both ends, causing the measured actuator displacement to be significantly greater than the vertical displacement of the aluminum alloy members themselves. Therefore, displacement transducers were installed on the aluminum alloy members to measure the relative vertical displacement between the upper and lower ends.

To measure the relative vertical displacement between the upper and lower ends of the aluminum alloy members, linear variable displacement transducers were fixed to the upper end using clamps. The connection between the displacement transducers and clamps adopted a hinged installation method. This hinged configuration served two critical functions: first, it allowed the displacement transducer to move horizontally with the member when lateral displacement occurred due to buckling; second, it enabled the displacement transducer to rotate freely, maintaining a vertical measurement direction. This design ensured complete synchronization between the displacement transducer and the deformation trajectory of the member while maintaining measurement reference stability, allowing precise measurement of relative vertical displacement during buckling.

Fig. 4 shows the schematic of the displacement and strain measurement point layout. Each specimen was equipped with four displacement transducers. The displacement transducers had a measurement range of 0–50 mm and an accuracy of ±0.01 mm, calibrated against a micrometer prior to testing. D1 and D2 were vertical displacement transducers symmetrically arranged along the central axis on the outer side of the flanges. As mentioned earlier, D1 and D2 measured the relative vertical displacement between the upper and lower ends of the aluminum alloy members. The average of the two readings was taken as the relative displacement of the members. D3 and D4 were horizontal wire displacement transducers fixed to the ground via brackets, with the wire ends attached to the web at the center of the aluminum alloy members to measure horizontal displacement at the midpoint. This data was used to determine residual deformation.

Six unidirectional strain gauges were affixed to the specimens, labeled S1 to S6, all located on the central cross-section of the members. S1 to S4 were symmetrically placed at the outer corner points of the flanges, while S5 and S6 were affixed to the web, 30 mm from the inner side of the flange. These six strain measurement points served two main purposes: first, to determine whether the specimen was loaded centrally during the preloading phase based on the measured strain data; second, to assess the tensile condition of the member during loading, preventing premature fracture.

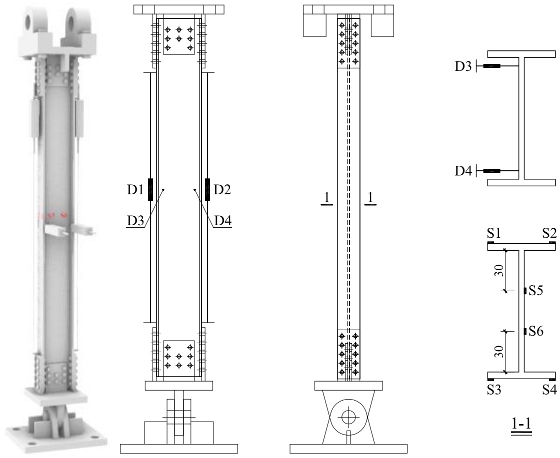

Fig. 4 Schematic of measurement point layout

2.2. Result of the experiment

Taking specimen L1000-TestA as an example, the hysteretic loading process is illustrated in Fig. 5. The loading protocol (Fig. 5(a)) was displacement-controlled by the actuator, with positive displacement applying compression and negative displacement applying tension. Each loading cycle consisted of compression loading, unloading, tension loading, and unloading. Residual deformation was observed after each cycle, with the actuator deviating from its initial position upon unloading.

To illustrate the load-displacement variation during loading, one cycle A-B-C-D-E from the hysteretic loading process is discussed. Fig. 5(b) shows the load-displacement hysteresis curve measured by the actuator, where a slip was observed near the zero-load point due to the finite stiffness of the reaction frame and connection components, as well as slip between various connectors. Fig. 5(c) presents the load-displacement curve based on the vertical relative displacement between the aluminum alloy member and the upper and lower end connections, reflecting the intrinsic hysteretic behavior of the aluminum alloy member. Fig. 5(d) displays the horizontal displacement at the midpoint of the specimen, including the member's deformation and rigid body horizontal displacement induced by end rotation.

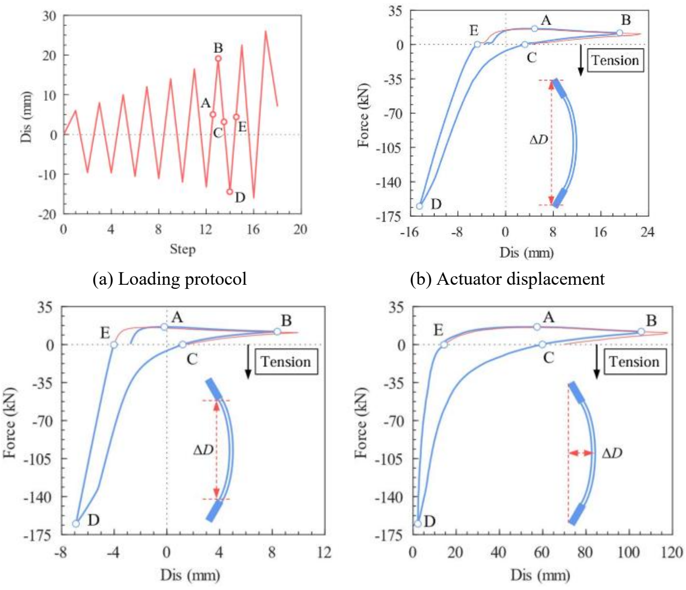

(a) Loading protocol (b) Actuator displacement

(c) Vertical relative displacement (d) Horizontal displacement at the midpoint

Fig. 5 Example of hysteretic loading (L1000-TestA)

Point A represented the compression extreme. After passing point A, the member buckled, resulting in a reduction in bearing capacity along segment A-B. Segment B-C corresponded to negative displacement increase (compression unloading). At point C, the load returned to zero, yet notable residual deformation remained in both vertical and horizontal directions. In segment C-D, the specimen was subjected to tension, where plastic deformation partially alleviated residual deformation caused by compression. Segment D-E represented the tension unloading phase. Upon tension unloading to zero, elastic deformation recovery occurred, causing the member to lengthen slightly compared to the pre-compression loading phase. The horizontal deformation was essentially consistent with the pre-compression loading phase. Since horizontal residual deformation was similar, no significant reduction in bearing capacity was observed in the subsequent hysteretic loading cycle.

Fig. 6 illustrated the deformation of specimens L1200-TestA and L500-TestB before loading and at the final loading stage. The hysteresis curves for some specimens are presented in Fig. 7, due to space constraints. The experimental data indicated that members with lower slenderness ratios exhibited higher degrees of plastic deformation under the same loading displacement, resulting in more significant residual deformation upon unloading. Members with lower slenderness ratios demonstrated fuller hysteresis curves and better energy dissipation capacity.

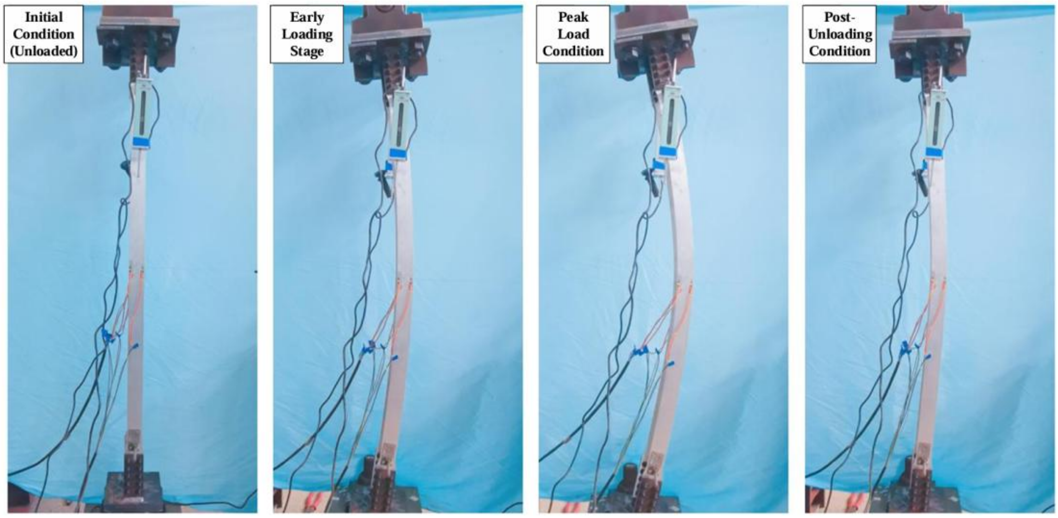

(a) Deformation of L1200-TestA

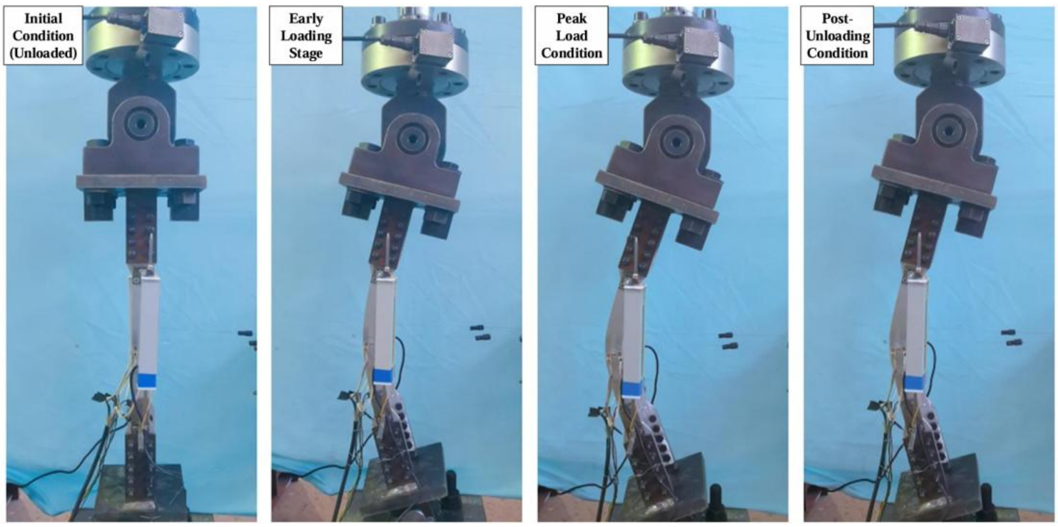

(b) Deformation of L500-TestB

Fig. 6 Deformation of specimens

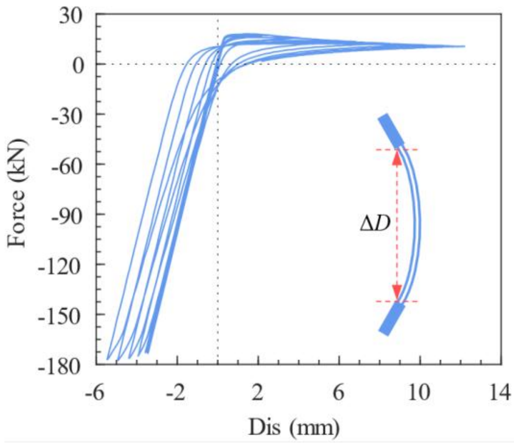

(a) Vertical displacement of L1200-TestA

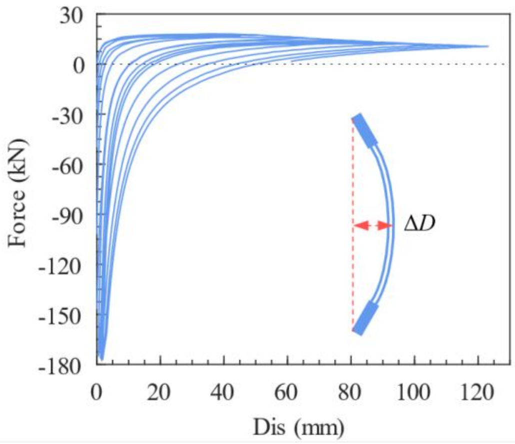

(b) Horizontal displacement of L1200-TestA

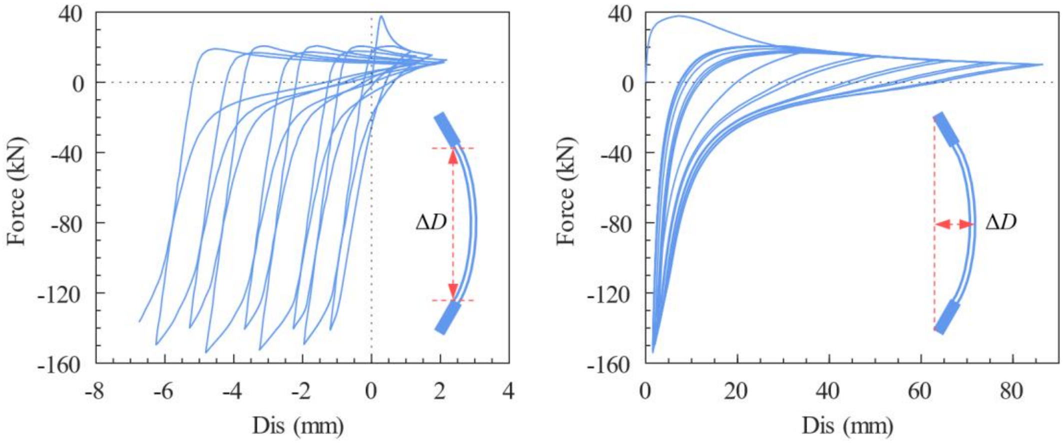

(c) Vertical displacement of L500-TestB (d) Horizontal displacement of L500-TestB

Fig. 7 The hysteresis curves of specimens

3. Numerical simulation

3.1. Finite element model

The FE model was developed using the general finite element software ABAQUS, with member dimensions consistent with the test specimens. Since the end connections are not the primary focus, bolts and bolt holes were assigned the same diameter to simplify computation. With reference to Article 12.2.4 of the Code for Design of Aluminum Structures [33], an initial imperfection amplitude of $L/1000$ was considered for the aluminum alloy members, where L represents the member length. This value was selected to reflect typical geometric imperfections observed in practical engineering applications, ensuring the model accurately captures the potential buckling behavior of the members. A buckling analysis was first conducted to determine the buckling mode of the member. The first mode exhibited a sine half-wave buckling around the weak axis, which was used as the initial geometric imperfection distribution. This imperfection was applied by modifying the nodal coordinates of the elements.

The cyclic constitutive model of aluminum alloy was based on the Chaboche model, selected for its capability to accurately capture cyclic hardening and ratcheting effects under cyclic loading. Material parameters are defined in Table 3. Parameters σ_0, Q_∞ and b represent isotropic hardening parameters, while C_k and Υ_k denote kinematic hardening parameters. The FE model contained multiple contact pairs. The upper and lower ends and connecting plates were modeled as solids using C3D8R elements, an 8-node linear brick element with reduced integration suitable for contact analysis. The aluminum alloy members, being thin-walled structures, were modeled using S4R shell elements, a 4-node linear reduced integration shell element applicable to both thick and thin shells. The mesh distribution is shown in Fig. 8 (a), with uniform mesh division along the member's axial direction.

Table 3
Parameters of mixed hardening model

Parameter	σ_0	Q_∞	b	C_1	Υ_1	C_2	Υ_2	C_3	Υ_3	C_4	Υ_4
Value	233	28.7	4.8	8297	278	3501	146	3988	172	5194	190

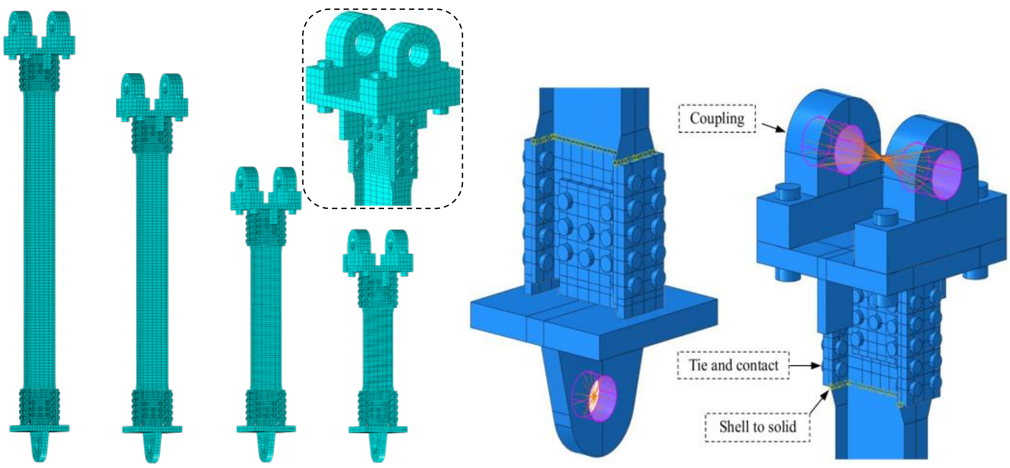

（a）Mesh division of FE models (b) The interaction and boundary conditions

Fig. 8 FE models

Fig. 8(b) illustrates the interaction and boundary conditions. A reference point (RP) was set at the actuator shaft center on the upper end of the member, bound to two circular hole surfaces. The RP point had constrained translational degrees of freedom (DoFs) in the X and Y directions, rotation about the strong axis, and torsional DoF. Vertical translation and rotation about the weak axis were released. All contact surfaces among the actuator loading head, upper end, connecting bolts, upper and lower connecting plates, and aluminum alloy flanges were set to hard contact in the normal direction and frictionless in the tangential direction. Binding constraints were applied between connecting plates and bolts, as well as between aluminum alloy flanges and bolts. The simplification assumes that the bolt diameter is equal to the hole diameter, which may underestimate the local stress concentration. However, the main purpose of this study is to evaluate the overall hysteretic performance and load-bearing capacity, so the simplification has limited impact on the overall results. The aluminum beam in the connecting section was modeled using solid elements, while the middle section used shell elements with shell-solid coupling. An RP point at the lower end hinge center was coupled with the hinge hole, constraining horizontal translation, rotation about the weak axis, and torsion while releasing vertical translation. A nonlinear spring was set between the RP point and the ground to account for stiffness and slip caused by reaction frames, supports, and gaps.

3.2. Numerical simulation results

For each numerical model, four displacement peak points were selected to plot the principal stress (σ_1) distribution. The stress distribution at peak points for specimens L1200-TestA and L500-TestB is shown in Fig. 9(a) and (b). Gray regions indicate yielding under compression or tension. The stress distribution shows tensile and compressive yielding in the mid-span section after buckling under compression. With larger bending amplitudes, a plastic hinge forms at the mid-span, causing plastic deformation mainly through hinge rotation, while other areas remain elastic and recover upon unloading. Shorter members exhibit a larger plastic region post-buckling. At tensile peak points, tensile yielding is observed in one flange, and full cross-sectional yielding may occur under sufficient tension. However, due to bolt-connected end holes reducing net cross-sectional bearing capacity, full cross-sectional tensile yielding is uncommon, generally only partially mitigating residual compressive deformation.

Experimental and simulated hysteresis curves of some specimens are compared in Fig. 9(c)-(f). The load-displacement curves from numerical simulations closely match the experimental results, with peak points and hysteresis shapes highly consistent. The maximum difference of peak point displacement and load value is less than 3%. The numerical results demonstrated that the adoption of shell elements combined with a mixed hardening material constitutive model achieved high computational accuracy, effectively capturing the stress states of structural members during the hysteretic loading process.

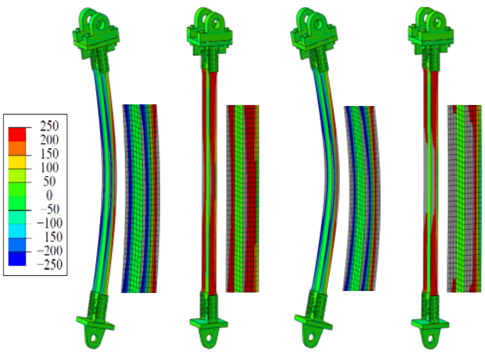

(a) Stress distribution of L1200-TestA

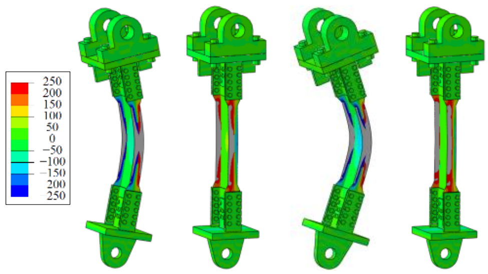

(b) Stress distribution of L500-TestB

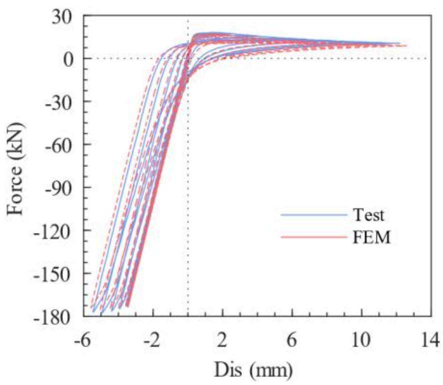

(c) Vertical displacement of L1200-TestA

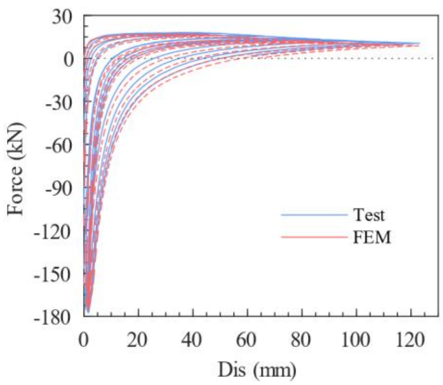

(d) Horizontal displacement of L1200-TestA

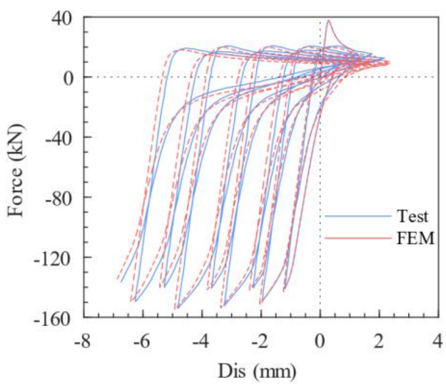

(e) Vertical displacement of L500-TestB

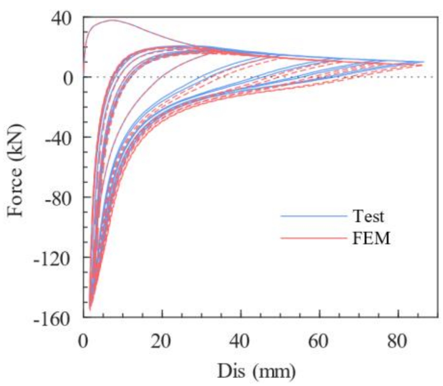

(f) Horizontal displacement of L500-TestB

Fig. 9 Numerical simulation results

4. Parametric analysis

4.1. Finite element model for pin-ended member

In the hysteretic experiment, aluminum alloy members were connected to the testing apparatus using bolts and connecting plates. The stiffness of the end connectors was significantly higher than that of the members, making the test essentially a hysteretic loading of pin-ended members with rigid zones. To further study the hysteretic behavior of aluminum alloy members, a pin-ended model was developed for parametric analysis, focusing on the effects of slenderness ratio, cross-sectional parameters, initial geometric imperfections, and tensile/compressive displacement amplitudes.

The pin-ended member FE model is shown in Fig. 10. RP points were set at the top and bottom centers, bound to the cross-section. The lower RP point released rotation about the weak axis while constraining other DoFs. The upper RP point released rotation about the weak axis and vertical translation while constraining other DoFs. The shell element type was S4R, chosen for its ability to accurately model both thick and thin shells while maintaining computational efficiency, with material parameters consistent with the previous model. Buckling analysis was performed by applying a vertical concentrated load at the upper RP point. The first global buckling mode was used as the imperfection distribution. Material and geometric nonlinearity were then considered for the hysteretic analysis, with vertical displacement applied at the upper RP point.

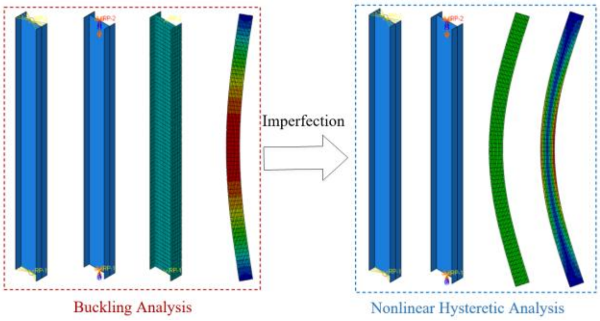

Fig. 10 FE models for pin-ended members

4.2. Effect of parameters

A FE model of pin-ended aluminum alloy members, as described previously, was established to perform a parametric analysis of hysteretic behavior. This study investigates the effects of geometric parameters and loading protocol parameters on hysteresis curves and stress distribution. Geometric parameters include slenderness ratio, cross-sectional parameters, and initial geometric imperfection. Loading protocol parameters encompass compressive displacement amplitude and tensile displacement amplitude. Each set of member parameters is shown in Table 4.

Table 4
Aluminum alloy member parameters

Slenderness Ratio	Cross-Section (mm)	Initial Imperfection Amplitude	Compressive Displacement Amplitude	Tensile Displacement Amplitude
50	H200×100×8×10	L/1000	0.01	-0.01
75	H200×100×8×10	L/1000	0.01	-0.01
100	H200×100×8×10	L/1000	0.01	-0.01
125	H200×100×8×10	L/1000	0.01	-0.01
150	H200×100×8×10	L/1000	0.01	-0.01
70	**H200×60×8×10**	L/1000	0.01	-0.01
70	**H200×80×8×10**	L/1000	0.01	-0.01
70	**H200×100×8×10**	L/1000	0.01	-0.01
70	**H200×120×8×10**	L/1000	0.01	-0.01
70	**H200×140×8×10**	L/1000	0.01	-0.01
70	H200×100×8×10	L/1000	0.01	-0.01
70	H200×100×8×10	L/500	0.01	-0.01
70	H200×100×8×10	L/200	0.01	-0.01
70	H200×100×8×10	L/100	0.01	-0.01
70	H200×100×8×10	L/50	0.01	-0.01
70	H200×100×8×10	L/1000	**0.005**	-0.01
70	H200×100×8×10	L/1000	**0.0075**	-0.01
70	H200×100×8×10	L/1000	**0.01**	-0.01
70	H200×100×8×10	L/1000	**0.0125**	-0.01
70	H200×100×8×10	L/1000	**0.015**	-0.01
70	H200×100×8×10	L/1000	0.005	**-0.004**
70	H200×100×8×10	L/1000	0.005	**-0.006**
70	H200×100×8×10	L/1000	0.005	**-0.008**
70	H200×100×8×10	L/1000	0.005	**-0.010**
70	H200×100×8×10	L/1000	0.005	**-0.012**

Hysteretic loading was applied in a single cycle, and the hysteretic relationship between the vertical displacement at the loading point and the load was extracted. The hysteresis curves of the members under various parameters are shown in Fig. 11. Downward vertical displacement at the loading point was considered positive, while upward displacement was negative.

Both load and displacement were normalized. The vertical axis of the hysteresis curve was defined as P/A, where P is the load and A is the cross-sectional area. The horizontal axis was defined as δ/L, where δ is the displacement at the loading point and L is the member length.

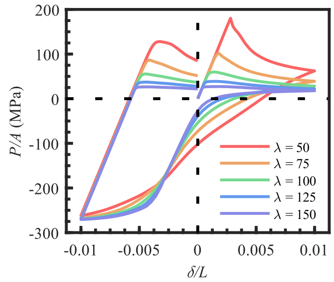

(a) Effect of slenderness ratio

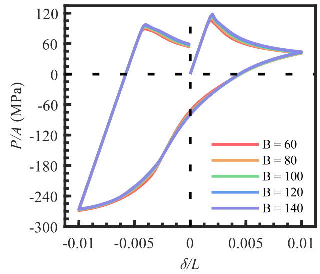

(b) Effect of cross-sectional parameters

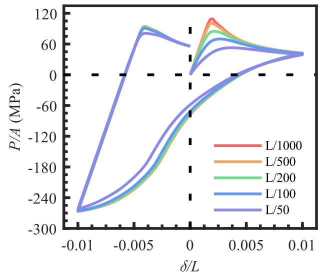

(c) Effect of initial imperfection

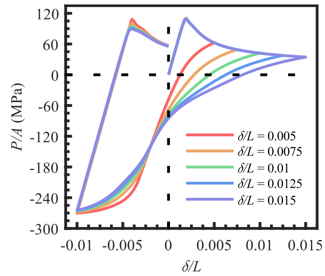

(d) Effect of compressive displacement amplitude

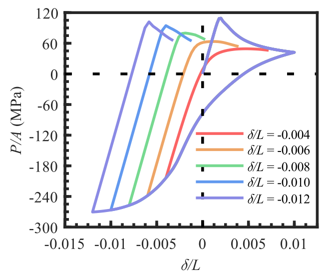

e) Effect of tensile displacement amplitude

Fig. 11 Parametric analysis results

4.2.1. Effect of slenderness ratio

In the first set of models, the cross-section was H200×100×8×10, the initial geometric imperfection amplitude was $L/1000$, the compressive displacement amplitude was 0.01, and the tensile displacement amplitude was -0.01. The slenderness ratios were 50, 75, 100, 125, and 150.

As shown in Fig. 11(a), with other parameters constant, higher slenderness ratios correspond to lower stable bearing capacity. Longer members with high slenderness ratios exhibit a gradual decrease in bearing capacity after buckling, with negligible residual deformation after unloading, indicating primarily elastic deformation. Conversely, shorter members with low slenderness ratios show a rapid decline in bearing capacity after reaching the peak load and exhibit significant residual deformation upon unloading.

4.2.2. Effect of cross-sectional parameter

In the second set of models, the slenderness ratio was 70, the initial geometric imperfection amplitude was $L/1000$, and the compressive and tensile displacement amplitudes were 0.01 and -0.01, respectively. The cross-section was H200×B×8×10, with member widths B ranging from 60 mm to 140 mm. It is worth noting that if the member length remains constant while the beam width changes, the radius of gyration of the cross-section will also change, leading to variations in the slenderness ratio. Therefore, the member lengths need to be calculated based on cross-sectional parameters to ensure a slenderness ratio of 70. As shown in Fig. 11(b), the hysteresis curves nearly overlap, indicating that cross-sectional parameters have negligible influence on hysteretic behavior.

This is mainly because, under a fixed slenderness ratio, the global buckling mode dominates the deformation process of H-section aluminum alloy members. In such cases, variations in sectional width do not significantly affect the overall stability or hysteretic response. However, this conclusion is valid only within the investigated range of slenderness ratios and loading conditions, and may not hold in cases where local buckling or interaction between local and global modes becomes critical.

4.2.3. Effect of initial geometric imperfection

In the third set of models, the slenderness ratio was 70, the cross-section was H200×100×8×10, the compressive displacement amplitude was 0.01, and the tensile displacement amplitude was -0.01. Initial geometric imperfection amplitudes were L/1000, L/500, L/200, L/100, and L/50.

As shown in Fig. 11(c), larger initial imperfection amplitudes intensify geometric nonlinearity during compression, reducing the stable bearing capacity. For members with larger imperfections, tangent stiffness decreases gradually during compression, with a smoother post-peak decline. In contrast, smaller imperfections exhibit sudden buckling with a rapid post-peak capacity drop.

4.2.4. Effect of compressive displacement amplitude

In the fourth set of models, the slenderness ratio was 70, the cross-section was H200×100×8×10, the initial geometric imperfection amplitude was L/1000, and the tensile displacement amplitude was -0.01. Compressive displacement amplitudes ranged from 0.005 to 0.015.

The effect of the compressive displacement amplitude on the hysteresis curves is shown in Fig. 11(d). Due to consistent geometric parameters, the hysteresis curves completely overlapped before buckling occurred. As the compressive displacement amplitude increased, the bending deformation became more pronounced, resulting in larger residual deformation after unloading. During the tensile phase, the hysteresis curves of all members converged at a fixed point, but the slope of the hysteresis curves passing through this point varied.

4.2.5. Effect of tensile displacement amplitude

In the fifth set of models, the slenderness ratio was 70, the cross-section was H200×100×8×10, the initial geometric imperfection amplitude was L/1000, and the compressive displacement amplitude was 0.01. Tensile displacement amplitudes ranged from -0.004 to -0.012. As shown in Fig. 11(e), the compression process remains consistent across amplitudes. Smaller tensile amplitudes result in less plastic deformation correction and larger residual deformation, corresponds to lower stable bearing capacity upon reloading. The stable bearing capacity of the member with a tensile displacement amplitude of -0.004 was significantly lower during reloading compared to the member with an amplitude of -0.012.

5. Simulation methods for aluminum alloy latticed shell member

5.1. Numerical simulation of independent member

In aluminum alloy latticed shells, the large number of members and their complex stress states result in multiple buckling modes under loading. Finite element method numerical models can better simulate the hysteretic behavior of these members. While solid and shell elements provide high computational accuracy, their efficiency is low and unsuitable for large latticed shell structures. Dividing members into multiple beam elements allows the simulation of both compressive buckling and tensile yielding.

Aluminum alloy members often feature an I-shaped cross-section, categorized as open thin-walled sections. Elements based on cross-sectional warping theory are more suitable for such profiles. Subsequent seismic response analysis of latticed shells was conducted using the ABAQUS finite element software, which offered various beam element types. Among them, the B32OS beam element is a three-dimensional beam element considering shear deformation and warping effects, making it ideal for simulating open thin-walled sections.

This section investigated the numerical accuracy of the B32OS beam element to derive an appropriate member simulation method. The numerical accuracy of the shell element had been experimentally validated and was thus used as a benchmark to evaluate the beam element's accuracy. Three loading methods were considered: weak-axis eccentric loading, strong-axis eccentric loading, and bi-axial eccentric loading. The member cross-section was H200×100×8×10, with slenderness ratios ranging from 50 to 120 about the weak axis. Boundary conditions at both ends were pin-ended along the strong and weak axes. The eccentric distances were 5 mm for the weak axis, 20 mm for the strong axis, and 5 mm and 20 mm for the weak and strong axes, respectively, in bi-axial loading. The members underwent a compression-first then tension loading protocol with maximum compressive displacement amplitude of 0.01 and tensile displacement amplitude of -0.08 under displacement loading. Partial hysteretic loading results are shown in Fig. 12, with subFig.s (a), (b), and (c) representing slenderness ratios of 60, 90, and 120, respectively. According to the hysteresis curves obtained from the shell and beam elements, the simulation accuracy for weak-axis, strong-axis, and bi-axial eccentric loading was high. The bearing capacity obtained from the shell element was slightly higher than that from the beam element, but the overall difference was minimal.

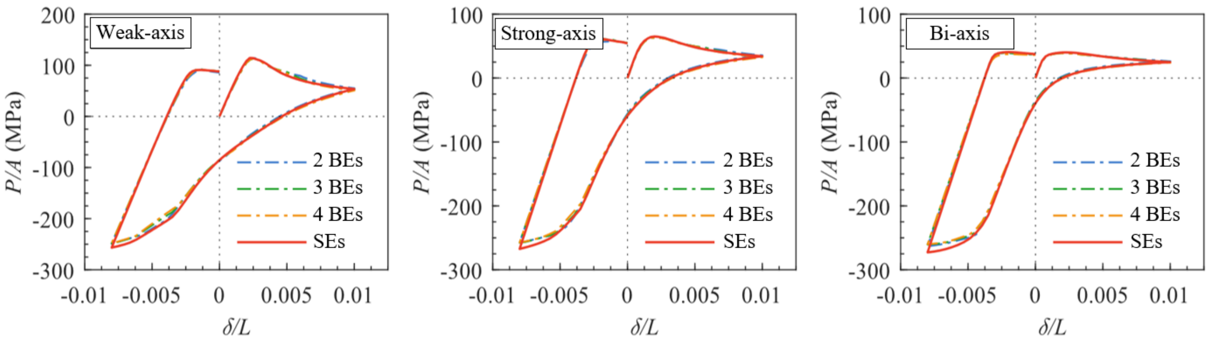

(a) Member slenderness ratio λ = 60

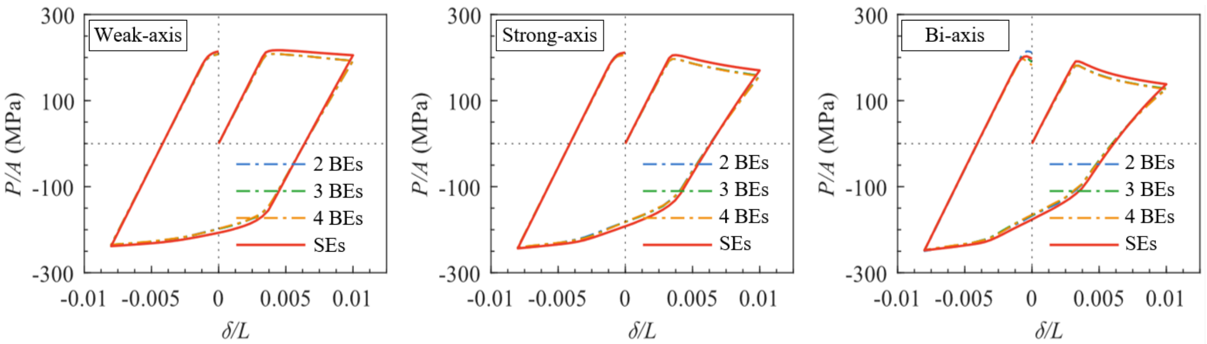

(b) Member slenderness ratio λ = 90

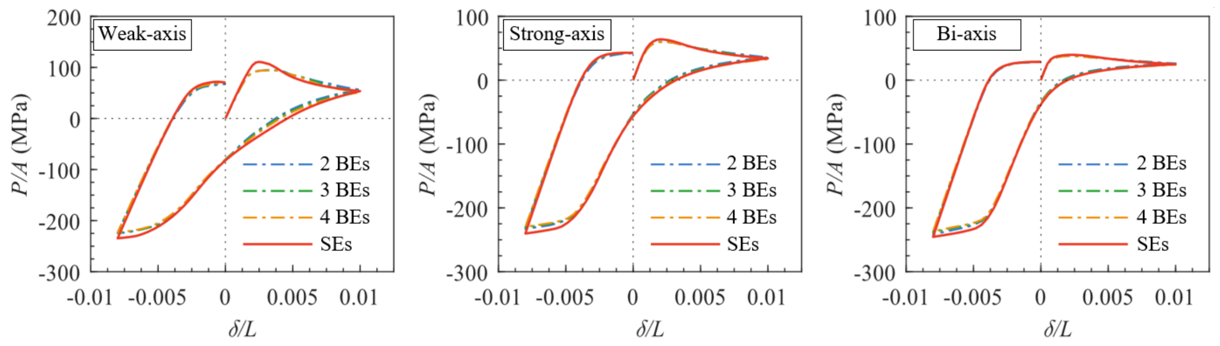

(c) Member slenderness ratio λ = 120

Fig. 12 Comparison of hysteresis curves between segmented beam elements and shell elements

Note: Weak-axis, Strong-axis, and Bi-axis denote weak-axis eccentric loading, strong-axis eccentric loading, and bi-axial eccentric loading, respectively. 2BEs, 3BEs, 4BEs represent segmented beam elements with 2, 3, and 4 elements, and SEs stands for shell elements.

Fig. 13 shows the impact of the number of member segments on computational accuracy. SubFig.s (a), (b), and (c) correspond to 2, 3, and 4 segments, respectively. The hysteretic loop area reflects the energy dissipation capacity of the members and serves as a comprehensive indicator of computational accuracy. The horizontal axis represents the hysteretic loop area calculated using beam elements, while the vertical axis represents the hysteretic loop area from shell elements. To facilitate comparison, the hysteretic loop area is normalized. The diagonal solid line indicates identical results from both element types; points above the line indicate higher results from shell elements, while points below suggest the opposite. The dashed lines represent a 5% error margin, with points within this range indicating less than 5% difference in results. As can be seen from the figure, almost all data points fall within the dashed line, indicating that the numerical accuracy of beam elements is high, with hysteretic loop area differences mostly within 5%. Moreover, as the B32OS element is a second-order beam element with high accuracy, the number of beam segments has minimal impact on results. Thus, when constructing the FE model of latticed shells, members can be divided into four beam elements.

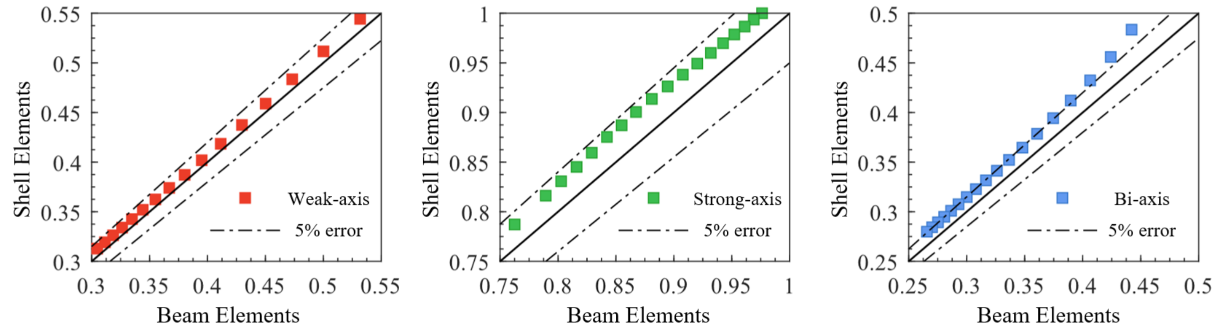

(a) Two member segments

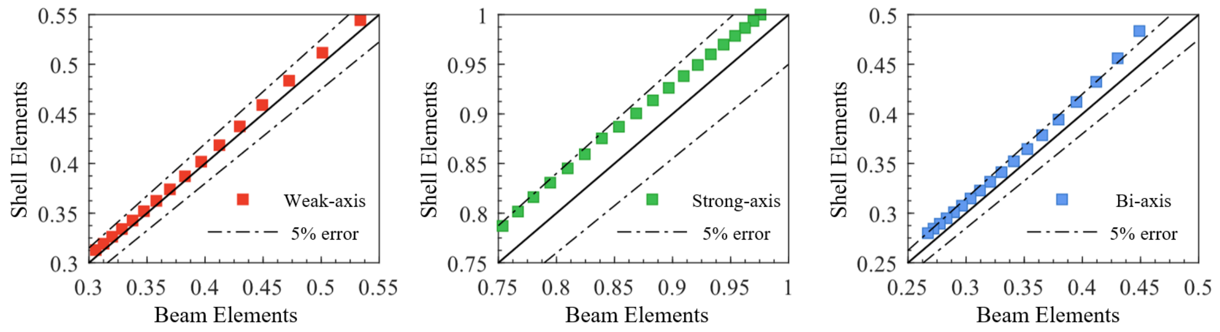

(b) Three member segments

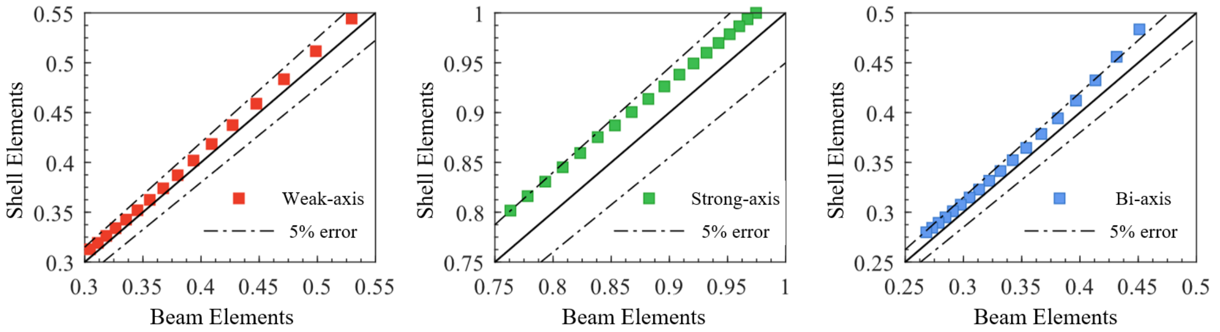

(c) Four member segments

Fig. 13 Impact of the number of member segments on computational accuracy

5.2. Numerical simulation of latticed shell member

The previous analysis showed that segmented beam elements produced results similar to shell elements, effectively simulating the hysteretic loading process. However, the boundary conditions in the prior study were pin-ended, differing from those of latticed shell members. Additionally, under seismic action, the stress state of latticed shell members is complex, with significant tension-compression asymmetry and bending moments and shear forces in both the strong and weak axes.

To further evaluate the simulation accuracy of beam elements for latticed shell members, a multi-scale latticed shell model was established, as shown in Fig. 14. Some members were simulated using shell elements, while the rest used beam elements with four segments per member. A full beam element latticed shell model was also constructed, and the axial displacement time-history curves of corresponding members were compared, as shown in Fig. 15. The displacement time-history curves obtained from both element types closely overlapped, indicating that the multi-segment beam element simulation results were reliable.

In addition to accuracy, the computational efficiency of the two models was also compared. The shell model contains more than 200% of the degrees of freedom of the beam model and requires approximately 2.5 times the computation time for the same analysis case. Since the beam model achieves comparable accuracy in simulating global hysteretic behavior while maintaining much lower computational cost, it is more suitable for large-scale structural analyses.

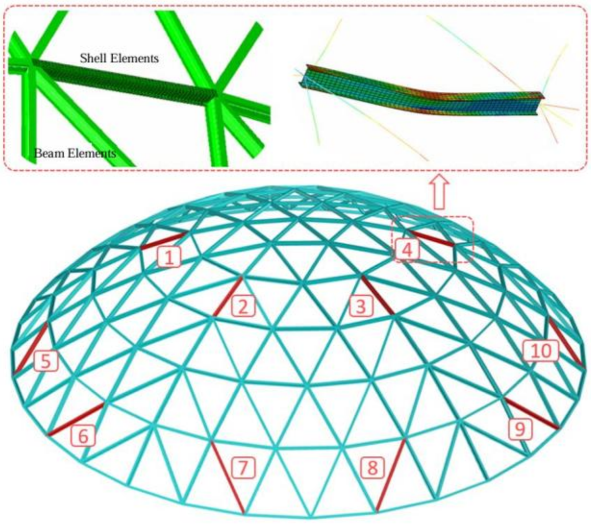

Fig. 14 Multi-scale latticed shell model

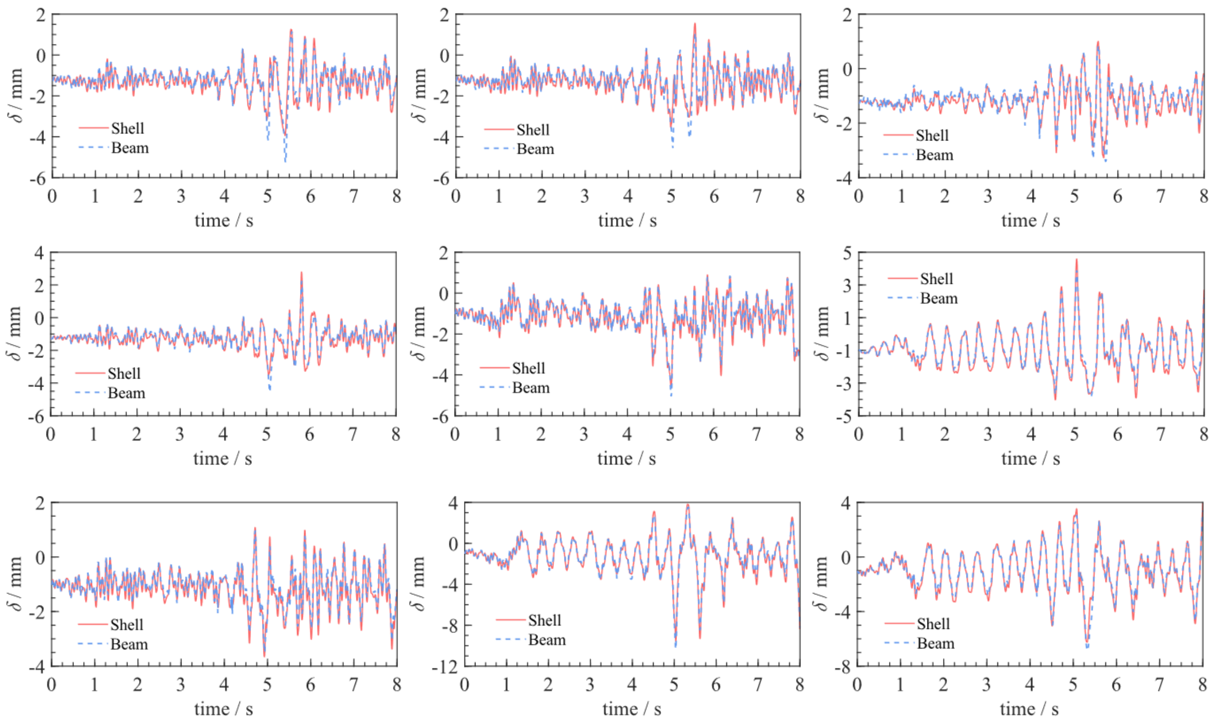

Fig. 15 Comparison of latticed shell member simulation results

6. Conclusions

This study investigated the hysteretic behavior of H-shaped aluminum alloy members commonly used in aluminum alloy gusset joint latticed shells. By combining experimental loading and numerical simulation methods, actual hysteresis curve data of aluminum alloy members were obtained, a refined FE model was established, and the impact of key parameters on the hysteretic loading process was analyzed. Finally, the applicability of beam elements in multi-scale latticed shell model was evaluated. The main conclusions are as follows:

(1) Hysteretic tests revealed that under cyclic loading, aluminum alloy members exhibit significant bearing capacity degradation after compression buckling. Tensile loading partially recovers residual deformation. Slenderness ratio significantly affects hysteretic behavior, with higher slenderness ratios

leading to more severe post-buckling bearing capacity degradation.

(2) Numerical results demonstrated that FE model employing shell elements and mixed hardening material constitutive models achieved high computational accuracy, accurately simulating the buckling process and hysteretic behavior of members, thus verifying the reliability of the numerical method.

(3) Parametric analysis indicated that slenderness ratio is a key parameter influencing hysteretic behavior. A higher slenderness ratio results in more pronounced post-buckling bearing capacity degradation. Increased initial geometric imperfection reduces stable bearing capacity. Larger compressive displacement amplitudes expand residual deformation and reduce stable bearing capacity upon reloading. Larger tensile amplitudes result in more plastic deformation correction.

(4) The multi-scale latticed shell model analysis showed that using a four-segment B32OS beam element effectively simulates the hysteretic behavior of members in latticed shells, with computational accuracy differing by less than 5% from shell element results.

This study fills the gap in hysteretic behavior research of aluminum alloy members under overall buckling conditions, providing essential experimental data and validated numerical analysis methods to support seismic design of aluminum alloy latticed shell structures.

Acknowledgements

This work was supported by the National Natural Science Foundation of China (grant number No. 51478335).

Reference

[1] Liu H, Ying J, Chen Z, et al. Research status of mechanical properties of aluminum alloy grid structure[C]//Structures. Elsevier, 2024, 61: 105967. https://doi.org/10.1016/j.istruc.2024.105967

[2] Sun Y. The use of aluminum alloys in structures: Review and outlook[C]//Structures. Elsevier, 2023, 57: 105290. https://doi.org/10.1016/j.istruc.2023.105290

[3] Osgood W R, Holt M. The Column Strength of Two Extruded Aluminum-Alloy H-Sections[J]. Technical Report Archive & Image Library, 1938.

[4] Holt M. Tests on built up columns of structural aluminum alloys[J]. Journal of Transportation Engineering, ASCE, 1940(105): 196-219. https://doi.org/10.1061/TACEAT.0005242

[5] Georgantzia E, Gkantou M, Kamaris G S. Aluminium alloys as structural material: A review of research[J]. Engineering Structures, 2021, 227: 111372. https://doi.org/10.1016/j.engstruct.2020.111372

[6] Guo X, Liang S, Shen Z. Experiment on aluminum alloy members under axial compression[J]. Frontiers of Structural and Civil Engineering, 2015, 9: 48-64. https://doi.org/10.1007/s11709-014-0271-9

[7] Liu H, Xiong Y, Chen Z, et al. Compressive performance of H-shaped aluminium alloy members with web openings[J]. Engineering Structures, 2022, 266: 114595. https://doi.org/10.1016/j.engstruct.2022.114595

[8] Xiong Y, Liu H, Chen Z, et al. Flexural performance of H-shaped aluminium alloy members with web openings[J]. Thin-Walled Structures, 2023, 185: 110627. https://doi.org/10.1016/j.tws.2023.110627

[9] Zhu S, Guo X, Liu X, et al. The in-plane effective length of members in aluminum alloy latticed shell with gusset joints[J]. Thin-Walled Structures, 2018, 123: 483-491. https://doi.org/10.1016/j.tws.2017.10.033

[10] Sun G, Li B, Wu J. Mechanical performance analysis method for ribbed H-section aluminum alloy members with initial curvature and torsion angle[J]. Thin-Walled Structures, 2025, 206: 112662. https://doi.org/10.1016/j.tws.2024.112662

[11] Wang Y Q, Yuan H X, Chang T, et al. Compressive buckling strength of extruded aluminium alloy I-section columns with fixed-pinned end conditions[J]. Thin-Walled Structures, 2017, 119: 396-403. https://doi.org/10.1016/j.tws.2017.06.034

[12] Yuan H X, Wang Y Q, Chang T, et al. Local buckling and postbuckling strength of extruded aluminium alloy stub columns with slender I-sections[J]. Thin-Walled Structures, 2015, 90: 140-149. https://doi.org/10.1016/j.tws.2015.01.013

[13] Wang Z X, Wang Y Q, Sojeong J, et al. Experimental investigation and parametric analysis on overall buckling behavior of large-section aluminum alloy columns under axial compression[J]. Thin-walled structures, 2018, 122: 585-596. https://doi.org/10.1016/j.tws.2017.11.003

[14] Adeoti G O, Fan F, Wang Y, et al. Stability of 6082-T6 aluminium alloy columns with H-section and rectangular hollow sections[J]. Thin-walled structures, 2015, 89: 1-16. https://doi.org/10.1016/j.tws.2014.12.002

[15] Čudina I, Skejić D. Extruded aluminium alloy members subjected to axial compression–A comprehensive review[J]. Engineering structures, 2025, 326: 119536. https://doi.org/10.1016/j.engstruct.2024.119536

[16] Guo X, Wang L, Shen Z, et al. Constitutive model of structural aluminum alloy under cyclic loading[J]. Construction and Building Materials, 2018, 180: 643-654. https://doi.org/10.1016/j.engstruct.2024.119536

[17] Pisapia A, Nastri E, Piluso V, et al. Experimental campaign on structural aluminium alloys under monotonic and cyclic loading[J]. Engineering Structures, 2023, 282: 115836. https://doi.org/10.1016/j.engstruct.2023.115836

[18] Branco R, Costa J D, Borrego L P, et al. Effect of strain ratio on cyclic deformation behaviour of 7050-T6 aluminium alloy[J]. International Journal of Fatigue, 2019, 129: 105234.

[19] Kourousis K I, Dafalias Y F. Constitutive modeling of Aluminum Alloy 7050 cyclic mean stress relaxation and ratcheting[J]. Mechanics Research Communications, 2013, 53: 53-56. https://doi.org/10.1016/j.ijfatigue.2019.105234

[20] Guo X, Zhu S, Liu X, et al. Experimental study on hysteretic behavior of aluminum alloy gusset joints[J]. Thin-Walled Structures, 2018, 131: 883-901. https://doi.org/10.1016/j.tws.2018.02.033

[21] Wu J, Li Y, Sun G, et al. Experimental and numerical analyses of the hysteretic performance of an arched aluminium alloy gusset joint[J]. Thin-Walled Structures, 2022, 171: 108765. https://doi.org/10.1016/j.tws.2021.108765

[22] Xu S, Chen Z, Wang X, et al. Hysteretic out-of-plane behavior of the Temcor joint[J]. Thin-walled structures, 2015, 94: 585-592. https://doi.org/10.1016/j.tws.2015.05.007

[23] Liu H, Li B, Chen Z, et al. Damage analysis of aluminum alloy gusset joints under cyclic loading based on continuum damage mechanics[J]. Engineering Structures, 2021, 244: 112729. 112729. https://doi.org/10.1016/j.engstruct.2021.112729

[24] Chen X, Zhang Z. Theoretical research on aluminium members under cyclic axial loading[C]//5th International Conference on Civil Engineering and Transportation. Atlantis Press, 2015: 226-229.

[25] Wu J, Zheng J, Sun G. Experimental and numerical analyses on aluminium alloy H-section members under eccentric cyclic loading[J]. Thin-Walled Structures. 2021, 162: 107532. https://doi.org/10.1016/j.tws.2021.107532

[26] Zhang Y, Luo Y, Guo X, et al. An updated parametric hysteretic model for steel tubular members considering compressive buckling[J]. Journal of Constructional Steel Research, 2021, 187: 106953. https://doi.org/10.1016/j.jcsr.2021.106953

[27] Dicleli M, Calik E E. Physical theory hysteretic model for steel braces[J]. Journal of structural engineering. 2008, 134(7): 1215-1228. https://doi.org/10.1061/(ASCE)0733-9445(2008)134:7(1215)

[28] Uriz P, Filippou F C, Mahin S A. Model for cyclic inelastic buckling of steel braces[J]. Journal of structural engineering (New York, N. Y.). 2008, 134(4): 619-628. https://doi.org/10.1061/(ASCE)0733-9445(2008)134:4(619)

[29] Sun G, Xiao S, Wu J, et al. Shaking table test and simulation on seismic performance of aluminum alloy reticulated shell structures under elastic and elastic-plastic stage[J]. Journal of Building Engineering, 2024, 97: 110878. https://doi.org/10.1016/j.jobe.2024.110878

[30] Sun G, Xiao S, Wu J, et al. Experimental and numerical simulation on seismic failure of aluminum alloy reticulated shell[J]. Journal of Constructional Steel Research, 2024, 221: 108905. https://doi.org/10.1016/j.jcsr.2024.108905

[31] GB/T 228-2002, Metallic Materials-tensile Testing at Ambient Temperature, 2002. (In Chinese).

[32] Shi Y P, Zhou Y. Detailed examples of ABAQUS finite element analysis[J]. 2006. (In Chinese).

[33] GB 50429-2007, Code for Design of Aluminium Structures, 2007. (In Chinese).